JOURNAL OF PROPULSION AND POWER
Vol. 26, No. 1, January–February 2010

Sensitivity of Turbine Efficiency and Flow Structures to Varying Purge Flow

P. Schuepbach* and R. S. Abhari†
ETH Zurich, 8092 Zurich, Switzerland
M. G. Rose‡
University of Stuttgart, 70569 Stuttgart, Germany
and
J. Gier§
MTU Aero Engines GmbH, 80995 Munich, Germany

DOI: 10.2514/1.44646

In many turbines, a small amount of air is ejected at the hub rim seal to prevent ingestion of hot gases into the cavity between the stator and the disk. This paper presents an experimental and computational investigation on the sensitivity of a 1.5-stage high-work axial turbine to varying purge flow rates equipped with nonaxisymmetric end walls. The paper gives a correlation of the total-to-total efficiency for different rates of purge flow injection while providing a physical explanation of the responsible mechanisms. The experimental data revealed a transitional behavior of the hub passage vortex when the purge flow injection rate reached 0.9% of the main mass flow. The increase of purge flow caused a lifting off of the rotor passage vortex. The result of this event was an unstable passage vortex resulting in a lower streamwise vorticity and higher unsteadiness. Additionally, a number of subharmonic frequencies appeared at an injection rate of 0.9% that were absent in the other injection rate cases. From the computations it could be seen that the injection created additional normal vorticity at the rotor leading edge. Through turning around the rotor leading edge, a streamwise vorticity component was introduced. The sensitivity to injection in terms of created vorticity was much larger below an injection rate of 0.9% than above.

Nomenclature

C	=	velocity, m/s
c_p	=	specific heat for constant pressure, J/kg
M	=	torque, Nm
$\dot{m}$	=	mass flow, kg/s
PR	=	$p/p_{t,\text{in}}$
p	=	pressure, Pa
$\bar{p}$	=	time mean part of pressure signal, Pa
$\tilde{p}$	=	periodic part of pressure signal, Pa
p'	=	random part of pressure signal, Pa
r	=	radial coordinate, m
S^2	=	strain rate, $1/s^2$
T	=	temperature, K
T	=	blade-passing period, s
t	=	time, s
U	=	blade speed, m/s
x	=	axial coordinate, m
Z	=	$(1 - \frac{p_{\text{trel,CFD}}}{p_{\text{trel,Meas.}}}) \cdot 100$, %
γ	=	ratio of specific heats
η	=	efficiency
θ	=	circumferential coordinate, rad
Π	=	pressure ratio
Ω	=	vorticity, 1/s
ω	=	rotational speed, rad/s

Subscripts

by	=	bypass
c, max	=	compressor maximum
cavity	=	cavity
dr	=	drum
in	=	inlet
$R1$ex	=	rotor1 exit
s	=	static flow quantity
t	=	stagnation flow quantity
$t$rel	=	relative frame stagnation flow quantity
$t$rot	=	rotary stagnation flow quantity not relative
tt	=	total to total
V	=	main venturi
$x_a v$	=	axially averaged rim seal exit
θ	=	circumferential coordinate
1.5	=	total to static 1.5 stages

I. Introduction

TO IMPROVE the thermal cycle efficiency of gas turbines, turbine entry temperatures have been continuously increased over the past decades. With these increases, gases into the disk cavities has become an issue, as it can cause overheating of the disks as well as thermal fatigue of the components. To mitigate the adverse effects of ingestion of hot gases, bypassed compressor air is injected through the rim seals between the rotating and stationary parts. The goal is to minimize the amount of injection mass flow and to reduce the aerodynamic losses, which can be attributed to the injection. The ingestion of hot gases is driven by disk pumping as well as by the external nonaxisymmetric pressure field. This has been experimentally investigated in previous studies; Kobayashi et al. [1] found that the pressure difference criterion underestimates the minimum cooling flow rate. Chew et al. [2] and Dadkhah et al. [3] also examined the question of the minimum coolant flow that is required to prevent ingestion and where the ingested air would end up in the cavity. The pressure field is, however, highly unsteady due to

Received 1 April 2009; revision received 5 July 2009; accepted for publication 16 July 2009. Copyright © 2009 by the American Institute of Aeronautics and Astronautics, Inc. All rights reserved. Copies of this paper may be made for personal or internal use, on condition that the copier pay the $10.00 per-copy fee to the Copyright Clearance Center, Inc., 222 Rosewood Drive, Danvers, MA 01923; include the code 0748-4658/10 and $10.00 in correspondence with the CCC.

*Research Assistant, Laboratory for Energy Conversion, ML J33, Sonneggstrasse 3; schuepbach@lec.mavt.ethz.ch.
†Professor, Laboratory for Energy Conversion, ML J33, Sonneggstrasse 3.
‡Senior Scientist, Institute of Aeronautical Propulsion.
§Senior Manager, Dachauer Strasse 665.

stator–rotor interactions. Roy et al. [4], for example, showed that the effect of the unsteady pressure field was much more pronounced inside the cavity than the time-averaged circumferential external pressure field. Recent research has focused on the flow interactions between the cooling air and the mainstream flow. McLean et al. [5,6] tested radial, impingement, and root injection cooling configurations. They observed that root injection had the most pronounced effect on the loss coefficient and total-to-total efficiency. Furthermore they found profound effects on the secondary flows of the following row. Girgis et al. [7] compared radial injection with compound injection, which had both radial and tangential components. They observed that the latter resulted in an efficiency improvement. Ong et al. [8] also concluded that some of the efficiency penalty due to coolant could be regained by introducing a swirl component to the coolant jet. Furthermore, they found that most of the coolant is entrained by the downstream blade hub secondary flow. Paniagua et al. [9] reported that there is an intensification of the rotor hub vortex and an enhancement of the radial migration due to injection. In recent studies, the importance of the unsteady interaction of the freestream and the cavity were highlighted. Boudet et al. [10] found frequencies that are unrelated to the blade-passing frequency. They attributed this to a nonlinear coupling of the blade-passing frequency with an instability formed inside the cavity. They concluded that only full annulus and unsteady modelling would capture the experimentally observed flow phenomenon. Reid et al. [11] quantified the efficiency penalty caused by the rim seal flow to be about 0.56% for 1.0% of injection mass flow. Marini and Girgis [12], in a numerical study, examined the effects of the blade leading-edge platform and noted that there is a 0.07% stage efficiency benefit and a reduced sensitivity to an increasing cavity mass flow.

In Schuepbach et al. [13], it was shown that the performance with purge flow decreases by 0.6% for 1% of purge flow. Furthermore, this work revealed an intensification of the secondary flows at the exit of the rotor as well as a higher penetration with purge flow. A spectral analysis at the exit of the rotor did show subharmonic frequencies of the blade-passing frequency with purge.

In this work, the results of four different injection rates are reported, including detailed measurements at the exit of the first stage of the 1.5 axial turbine. The first stage was equipped with nonaxisymmetric end wall profiles. The geometry is shown in Fig. 1. The contour range of the profile was $\pm 7\%$ span.

However, the focus of this work was not on the effect of end wall profiling, but on the influence of purge flow. For more details on the nonaxisymmetric design, refer to Germain et al. [14] or Schuepbach et al. [15]. In Schuepbach et al. [15], the response of the turbine with and without nonaxisymmetric end walls to purge flow injection was described.

II. Experimental Method

The experimental investigation was performed in LISA, the research turbine at the Laboratory for Energy Conversion at ETH Zurich. The 1.5 unshrouded high-work turbine designed by Behr et al. [16] was used for this study.

A. Experimental Turbine Facility

The air loop of the facility is quasi closed and includes a radial compressor, a two-stage water-to-air heat exchanger, and a calibrated venturi nozzle for mass flow measurements. Upstream of the turbine section is a 3 m flow conditioning stretch to ensure a homogenous flowfield. At the exit of the turbine section, the air loop opens to the atmosphere. A dc generator absorbs the turbine power and controls the rotational speed with an indicated accuracy of $\pm 0.02\%$ (± 0.5 rpm). The heat exchanger controls the inlet total temperature $T_{t,\text{in}}$ to an accuracy of $\pm 0.3\%$. A torque meter measures the torque on the rotor shaft. The turbine is unshrouded with a nominal tip gap of 0.7 mm, or 1% of the span.

a) First vane hub b) First vane tip c) Rotor hub

Fig. 1 Nonaxisymmetric end wall shapes from optimization.

Table 1 Relative uncertainty of FRAP probe

Yaw angle, %	Pitch angle, %	p_t, %	p_s, %
0.8	2.3	1	1.2

B. Measurement Technology

The unsteady flowfield was measured with a fast response aerodynamic probe (FRAP), which was developed at ETH Zurich (Kupferschmied et al. [17] and Pfau et al. [18]). The probe is capable of capturing unsteady flow features up to frequencies of 48 kHz based on measurements including total and static pressures, flow yaw and pitch angles, and Mach number. The frequency bandwidth of the temperature is limited to a frequency of 10 Hz. The influence of the measured temperature on the velocity is, however, very modest. The FRAP probe has a 1.8 mm tip diameter and is equipped with two sensors. The probe is operated in a virtual four-sensor mode to measure three-dimensional, deterministic, time-resolved flow properties. Table 1 gives the relative measurement uncertainties of the FRAP probe as a percentage of the calibration range of ± 30 deg for the angles and as a percentage of the dynamic head for the pressures.

The spatial resolution of the measurement grid consisted of 39 radial and 40 circumferential points (covering one stator pitch), with radial clustering near the end walls. The data were acquired at a sampling rate of 200 kHz over a period of 2 s, which corresponds to 4860 blade-passing events. The postprocessing was done for three consecutive rotor pitches. The temporal resolution was 82 points per blade-passing period.

C. Injection System

A new air system was designed to provide the possibility of injection of air through the rotor upstream rim seal. The air is bled off the primary air loop upstream of the flow conditioning stretch. The bleed air passes through a venturi to measure the bypassed mass flow. Finally, the bypass flow enters a plenum from which 10 separate tubes lead the flow to 10 nozzle guide vanes. Through these vanes, the flow enters the cavity labeled B in Fig. 2. From the cavity underneath the nozzle guide vanes, there are two leakage paths, indicated in Fig. 2 as dotted arrows P and S. One path is through the upstream rim seal into the main flow P. The rest of the gas is ejected through the drum to the ambient air after being measured in another venturi called the secondary mass flow S. The pressure difference over the labyrinth leading from the downstream rim seal into the drum is balanced. Under these conditions, the net mass flow through the downstream rim seal into the drum is assumed to be zero. Thus, the injection or

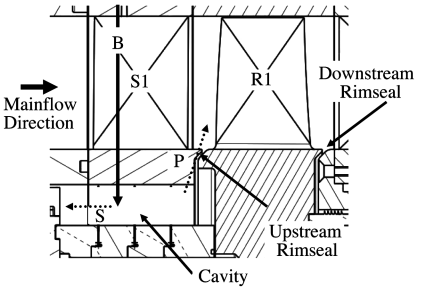

Fig. 2 Illustration of leakage path.

purge mass flow can be calculated as the difference of the bypass mass flow and secondary mass flow. Previously, it was only possible to run the rig with the upstream rim seal in an ingesting mode.

III. Experimental Results

A. Operating Conditions

During measurements, the turbine 1.5-stage total-to-static pressure ratio was kept constant at $\Pi_{1.5} = 1.65$. The entry temperature was kept constant to permit an accurate comparison of measurements made on different days. To account for the change in ambient pressure on different measurement days, the pressures were nondimensionalized by the respective inlet total pressure. The operating conditions are given in Table 2.

The purge flow is defined in terms of an injection rate (IR), which is given as follows:

$$\mathrm{IR} = \frac{\dot{m}_{\mathrm{by}} - \dot{m}_{\mathrm{dr}}}{\dot{m}_V} \cdot 100 \tag{1}$$

The tests were conducted for four different injection rates. At −0.1%, the rim seal was nominally in a modest ingestion mode, which is the standard operation condition of the turbine rig. Additionally, three injection cases with IR = 0.5, 0.9, and 1.3% were investigated. The purge flow wasn't preswirled.

B. Experimental Performance Sensitivity

In this section, the sensitivity of the total-to-total efficiency to different injection rates is presented. The definition of efficiency used in this study, accounting for the injection, is given as follows:

$$\eta_{\mathrm{tt}} = \frac{\frac{\varpi \cdot M}{\dot{m}_V \cdot c_p \cdot T_{t,\mathrm{in}}}}{1 - \left(1 - \frac{\mathrm{IR}}{100}\right) \cdot \left(\frac{p_{t,R1\mathrm{ex}}}{p_{t,\mathrm{in}}}\right)^{\frac{\gamma-1}{\gamma}} - \frac{\mathrm{IR}}{100}\left(\frac{p_{t,R1\mathrm{ex}}}{p_{t,\mathrm{in}}}\right)^{\frac{\gamma-1}{\gamma}}} \tag{2}$$

In the numerator, the power on the shaft measured with the torque meter is shown as the product of the rotational speed and torque. In the denominator, the isentropic work of the main flow (1 − IR) and the purge flow IR are determined. The measured efficiency sensitivity for four different injection rates is given in Fig. 3. In between IR = −0.1 and 0.5%, the rate of efficiency drop was 0.6% per percent injected mass flow. Between an injection rate of 0.5% and 0.9%, the slope increased to 1.0% per percent injection. Finally, between the highest two injection rates, the slope decreased again to 0.9% per injected mass flow percent.

The power of the turbine dropped almost linearly at 2% per percent of injected mass flow, as seen in Fig. 4. The total-to-total pressure ratio, which is also plotted in Fig. 4, dropped as well. The change in isentropic work was proportional to the total-to-total pressure ratio change. Hence, the efficiency dropped by less than 1%. The mechanism responsible for the reduction of the isentropic work was blockage due to the injected fluid and the losses it caused. The blockage of the rotor by this fluid caused the static pressure to rise at the rotor inlet by 0.57% for 1% of injected fluid. This resulted in a reduction of the first nozzle guide vane row exit Mach numbers by −1.2% per injected mass flow percent. The effect was not counteracted by a reduction of static pressure at the rotor exit as might be expected, indicating a reduction of capacity in the second vane also.

Table 2 Operating conditions, where rps refers to rounds per second

$\Pi_{1.5}$	$1.65 \pm 0.4\%$
$T_{t,\mathrm{in}}$, K	328 ± 0.2
$\frac{\dot{m}\sqrt{T_{t,\mathrm{in}}}}{p_{t,\mathrm{in}}}$, $\frac{\mathrm{kg\ K^{1/2}}}{\mathrm{s \cdot bar}}$	$152 \pm 0.2\%$
$\frac{N}{\sqrt{T_{t,\mathrm{in}}}}$, $\frac{\mathrm{rps}}{\mathrm{K^{1/2}}}$	$2.48 \pm 0.05\%$

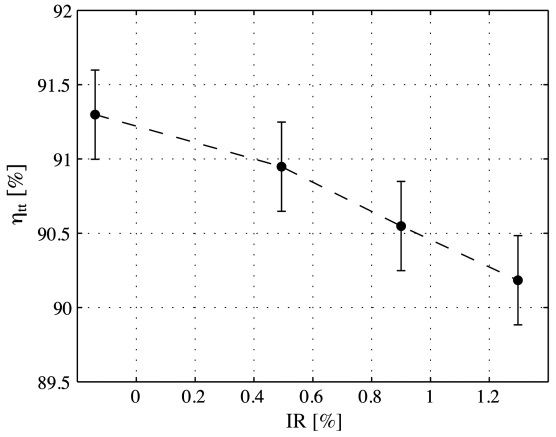

Fig. 3 Measured efficiency sensitivity to injection purge flow.

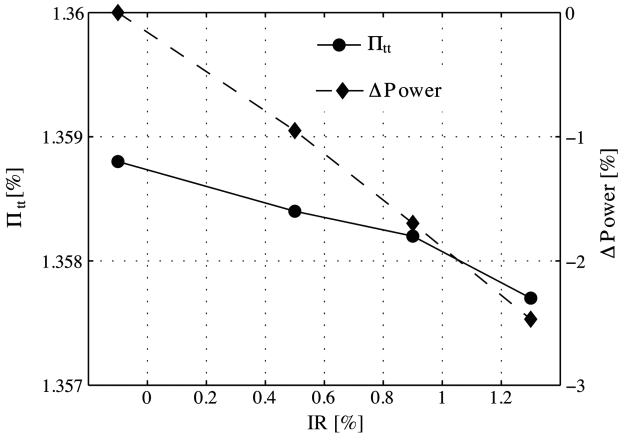

Fig. 4 Measured power drop and total-to-total pressure ratio.

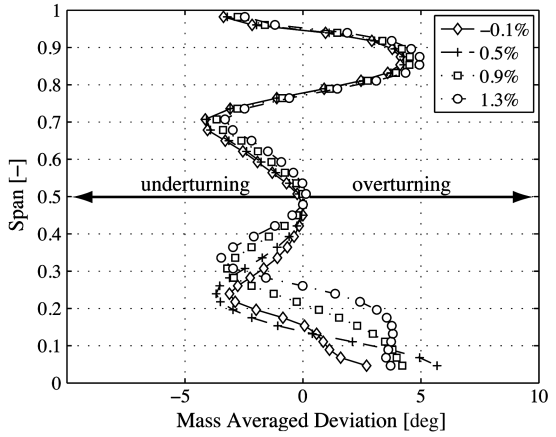

Fig. 5 Measured mass-averaged deviation at rotor exit.

C. Influence of Injection Rate at Rotor Exit

Figure 5 shows the circumferentially mass flow averaged deviation from the midheight relative flow yaw angle at the exit of the rotor. The design metal angle is −67 deg over the whole span. The flowfield at the rotor exit was very three dimensional. At 72% span, the tip passage vortex introduced underturning. At 88% span, there was the combined overturning of the tip passage vortex and the tip leakage vortex. Finally, at the casing the underturning part of the tip leakage vortex can be seen. In the outer half of the annulus, the influence of the injection is 0.5 deg more turning with an injection rate of 1.3%. At the hub one can see the underturning region between

20 and 30% span and the overturning near the hub. At the hub the influence of the injection was pronounced. If the injection was applied going from IR = −0.1 to 0.5%, the overturning was increased by 3 deg, whereas the underturning was increased by 0.5 deg. When the injection was further increased by 0.4% to an injection rate of IR = 0.9%, the overturning reduced by almost 2 deg, while the amount of underturning did not change. However, the maximum underturning was radially further out by about 7% of the span height. At the highest injection rate of 1.3%, the overturning reduced by another 0.5 deg, whereas the underturning increased by the same amount. The underturning location was 2.3% span further out than with the 0.9% injection rate, and the overturning was even 8.6% span further out.

The radial distribution of the total-to-total efficiency is shown in Fig. 6. It should be noted that this efficiency is linearly related to the total pressure distribution because the power used to calculate it is only a one-dimensional value coming from the torque tube and is not based on a total temperature profile. Therefore, the efficiency in the outer half is linearly decreasing with increasing injection although the total-to-total pressure ratio is not changing. However, the one-dimensional power is dropping linearly, as seen in Fig. 4. There was an increasing efficiency deficit toward the hub for the injection case. With the small suction of IR = −0.1%, the efficiency plot showed no distinct loss region at the hub as a result of the nonaxisymmetric end wall profiling. If a 0.5% purge flow was used, a clear loss region reappeared. If the purge flow was increased to an injection rate of 0.9%, the size of the loss core, seen as a deficit of efficiency in Fig. 6, increased considerably, leading to an increased loss of efficiency per injected mass flow, as seen in Fig. 3. At the maximum injection rate of 1.3%, the loss core at the hub decreased further with a 2.5% lower minimum. When the injection was increased from IR = 0.5 to 0.9%, the hub efficiency minimum moved out by 8.6% of the span height. If the injection was increased by the same amount again, to IR = 1.3%, the movement was only 4.3% of the span height.

Figure 7 shows the experimental streamwise vorticity at the rotor exit time averaged in the rotating frame of reference for the four different injection rates. In the outer half of the annulus, there is hardly any difference between the four cases; therefore, the discussion focuses on the lower half only. In this region, two vortical structures of the opposite sign could be detected. The larger one with positive vorticity A was the rotor hub passage vortex. Just to the left was the trailing shed vortex B. If a 0.5% purge flow was applied, the hub passage vortex center moved 10% of the span closer to the hub compared with the suction case of IR = −0.1%. At the same time, the integrated circulation increased by 75%. The integrated circulation of the trailing shed vortex increased by 23%. The trailing shed vortex center remained at about the same position independent of the injection rate. If the injection rate was increased to IR = 0.9%, the integrated circulation of the hub passage vortex fell by 12% relative to the IR = 0.5% case. At the same time, the hub passage vortex center rose again by 10% span height. The trailing shed vortex integrated circulation remained the same. At the maximum injection rate of 1.3%, the integrated circulation of the passage vortex increased again by 8% and the vortex center was another 10% span height further out. The integrated circulation of the trailing shed vortex increased by 10%.

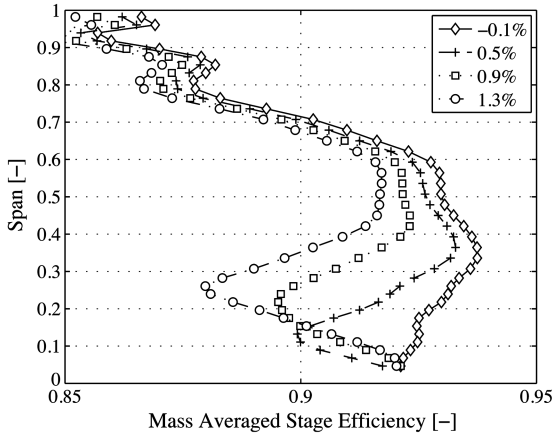

Fig. 6 Measured mass-averaged efficiency for different injection rates.

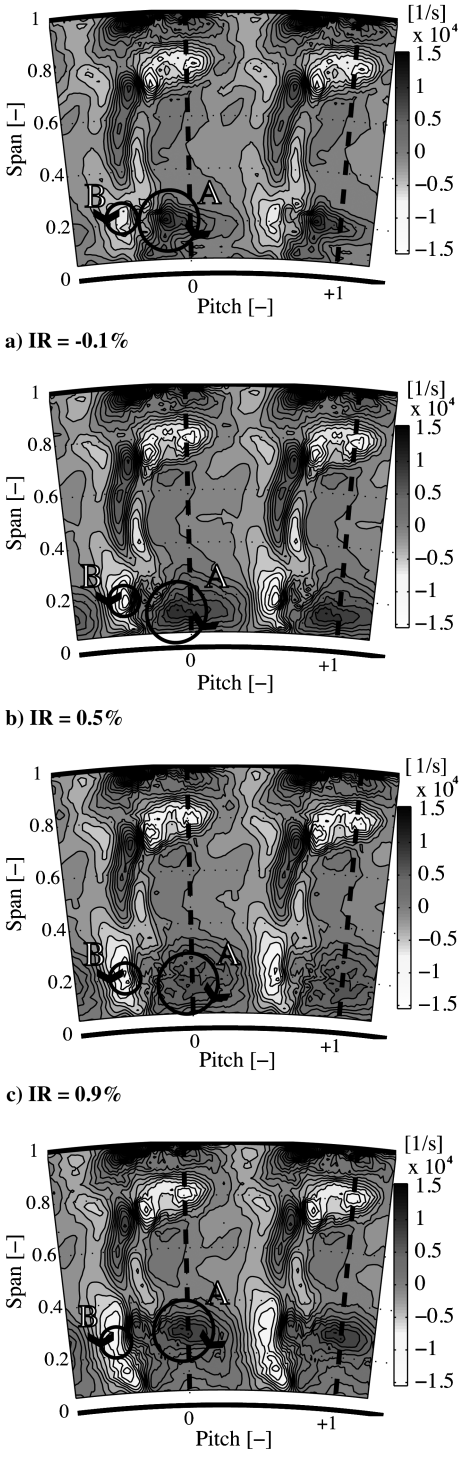

Fig. 7 Measured time-average streamwise vorticity in the rotor frame of reference at traverse plane *R*1ex.

The rms values of the random part of the total pressure signal gives a measure of the unsteadiness. Using the triple decomposition of the time-resolved pressure signal as shown in Eq. (3), the random part $p'(t)$ can be evaluated as the difference between the time-resolved pressure $p(t)$ and the phase-locked averaged pressure $\bar{p} + \tilde{p}(t)$:

$$p(t) = \bar{p} + \tilde{p}(t) + p'(t) \tag{3}$$

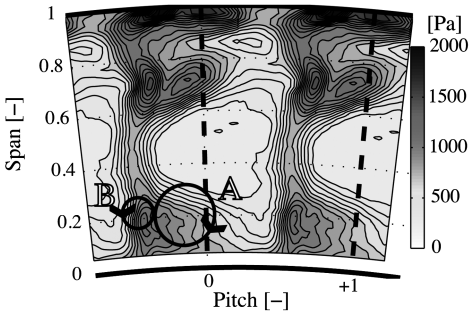

a) IR = -0.1%

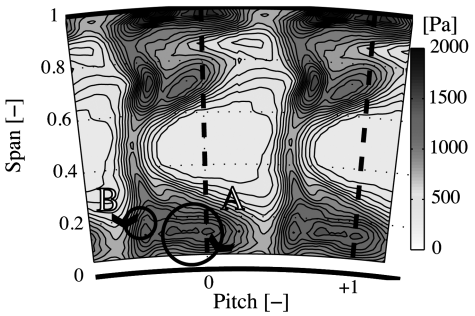

b) IR = 0.5%

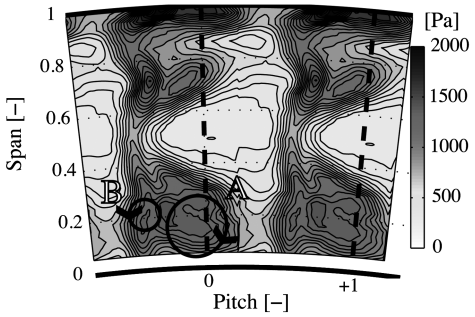

c) IR = 0.9%

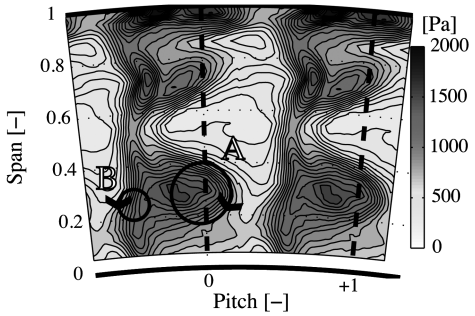

d) IR = 1.3%

Fig. 8 Measured time-average rms of total pressure random part in the rotor frame of reference at traverse plane *R*1ex.

The same approach was used by Porreca et al. [19] to derive turbulent quantities. Figure 8 shows the time-averaged rms values of the random part of the total pressure signal in the rotating frame of reference. In the suction case of IR = −0.1%, unlike the injection cases, there was only one rms peak at the hub. If a 0.5% mass flow was injected, the integrated rms rose by 33%. If the injection was increased to 0.9%, the integrated rms rose by another 16%. The increase was only the result of an increased area, as the peak rms value remained the same. In the IR = 1.3% case, the hub passage vortex was leaving the end wall and the covered area was slightly decreasing, resulting in a 3.5% lower integrated rms value.

The frequency composition of the flow in the hub loss core was determined from a fast Fourier transform (FFT) of the raw voltage signal of sensor 1 of the FRAP probe, which was directly related to the pressure signal. The amplitude was nondimensionalized by the baseline value at blade-passing frequency. The measurements at 16% span and −12.5% pitch were considered. The results are presented in Fig. 9. The blade-passing period was 2430 Hz. With the IR = −0.1% case, there was a distinct peak at the blade-passing frequency. With an injection rate of 0.9% flow, the peak amplitude at the blade-passing frequency was reduced. Furthermore, a band of subharmonics of the blade-passing frequency appeared. The same observation was made in Schuepbach et al. [13] for an axisymmetric geometry. However, this investigation showed that these subharmonics are only present at the particular injection rate of 0.9%.

IV. Time-Resolved Computational Model

A. Grid and Boundary Conditions

The grid used for the time-resolved simulations was the same one used during the design phase. As the ratio between vanes and blades was 2:3, two vane passages of the first and second vane row as well as three rotor passages were represented with periodic boundary conditions in the circumferential direction. To have a realistic rim seal flowfield, the physical cavity space as seen in Fig. 2 underneath the first vane row was fully discretized with an interface to the first vane row hub end wall. A meridional grid plane is shown in Fig. 10. The total number of grid nodes was 10.8×10^6. The nondimensionalized wall distances on the airfoils and the end walls were about $y^+ = 1$. At the inlet of the domain, a constant total pressure of 1.4 bar and a constant total temperature of 55°C were applied. At the exit, the measured mass flow for these inlet conditions was set. The cavity inlet was either modeled as a wall or with an inlet mass flow of

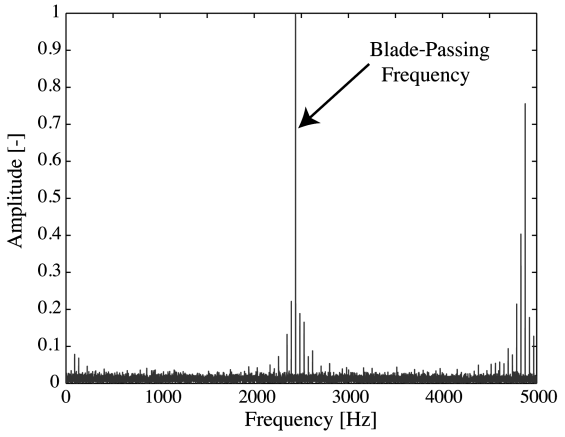

a) IR = -0.1%

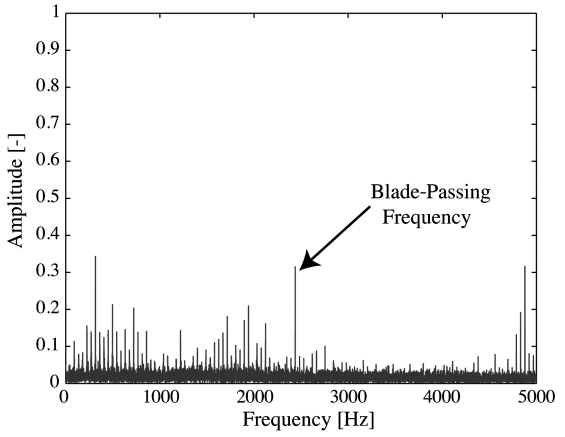

b) IR = 0.9%

Fig. 9 FFT of the measured raw voltage signal of the FRAP probe at 16% span and −12.5% pitch.

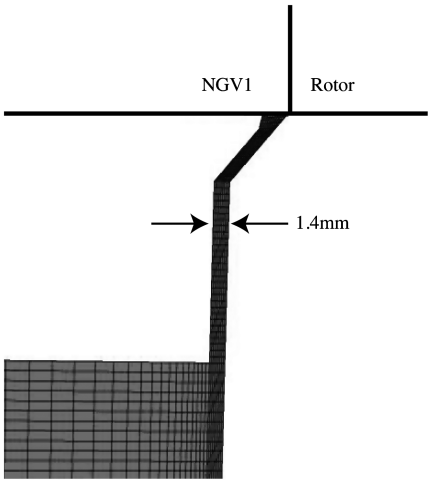

Fig. 10 Meridional grid plane of cavity.

0.9% of the main mass flow. The cavity fluid temperature was set to 50°C, as measured in the rig.

B. Solver

In contrast to the design calculations, the time-resolved results were achieved with the commercial ANSYS CFX V11.0 software package. A steady run was done to derive the initial conditions for the unsteady simulation. The temporal resolution was 20 steps per blade-passing event. This yielded a 0.33 deg shift of the rotor per time step. For this simulation, the k–ε turbulence model was used. The maximum residuals were found to be in the order of 10^{-3}, while the mass imbalances were in the order of 10^{-5}. The periodic convergence of the unsteady simulations was judged based on the correlation coefficient of two pressure monitoring points at the exit of the rotor row. Two consecutive vane passage pressure events had to reach a correlation coefficient of above 99%.

C. Validation

To validate the computational model, the time-averaged results of the calculation were compared with the experimental data. The validation was done for the cases of IR $= -0.1$ and 0.9%. As an example, the normalized relative total pressure at the rotor exit time averaged in the relative frame is shown in Figs. 11 and 12. Generally, Figs. 11 and 12 show the three zones of low relative total pressure caused by the hub and tip secondary flow as well as by the tip leakage vortex. The shape and radial position of the loss cores were well predicted. Figure 11 shows good qualitative agreement between the computation and the experiment, which is also confirmed by the quantitative comparison as shown in Fig. 13a. The radial position of the loss cores was especially well captured by the computation. When purge flow was applied, the loss core at the hub grew considerably as a consequence of the injection, as seen in Fig. 12. The hub loss core was radially further out compared with the IR $=$ -0.1% case. All these trends were captured in the computational model. The relative error for both operating conditions is given in Fig. 13. The loss in the tip leakage and tip passage vortex was overpredicted by about 6% with and without leakage. In the wake region, the mismatch was below 5%. In the hub passage vortex region, the error was within 1% without injection and within ± 3% with injection. In the freestream region, the computation overpredicted the relative total pressure by about 1%. Based on these observations, a high level of confidence can be placed on the interpretations of the computed flowfield.

D. Computational Results

The pressure at the exit of the rim seal is assumed to vary much more than inside the cavity. Therefore, the static pressure field at the exit of the rim seal shows the regions where there is ingestion and ejection. Where the pressure is low, the rim seal will inject and, where

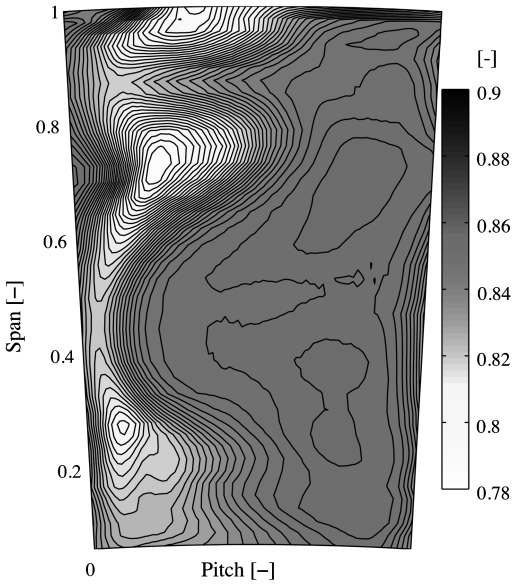

a) Measured

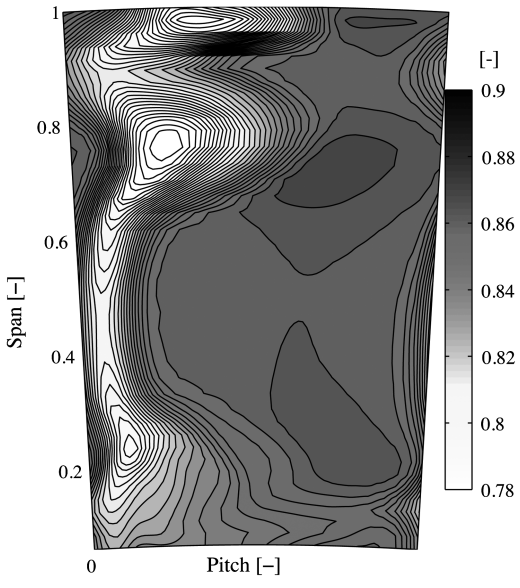

b) Computation

Fig. 11 Comparison of nondimensional relative total pressure for the computation and experiment at rotor exit IR $= -0.1$%.

it is high, the rim seal will ingest. In Fig. 14, the axially averaged circumferential static pressure distribution at the rim seal exit is plotted against time for the three injection cases over two vane pitches. Inclined structures in this presentation are associated with the rotor blades, whereas vertical structures are the result of the vane pressure field. It could be seen that the rotor dominates the rim seal exit pressure field. However, the influence of the vanes leads to a modulation of the inclined low- and high-pressure traces. The vane to blade ratio is 2:3. The IR $= 0.5$% case showed three high-pressure and three low-pressure regions, which represented the first blade-passing harmonic. In the IR $= 0.9$% case, a second harmonic appeared in the time–space diagram. At the highest injection rate of 1.3%, the influence of the second harmonic was reduced. If the injection rate was increased, the intensity of the low-pressure regions was reduced. This is the result of a feedback mechanism. When a jet left the rim seal, the pressure in front of the jet increased as a result of streamline curvature as a consequence of the introduced blockage. Figure 15 shows an illustration of the effect of additional blockage caused by the injection jet. In the IR $= 0.9$% case, the inclined low-pressure zone is modulated the least.

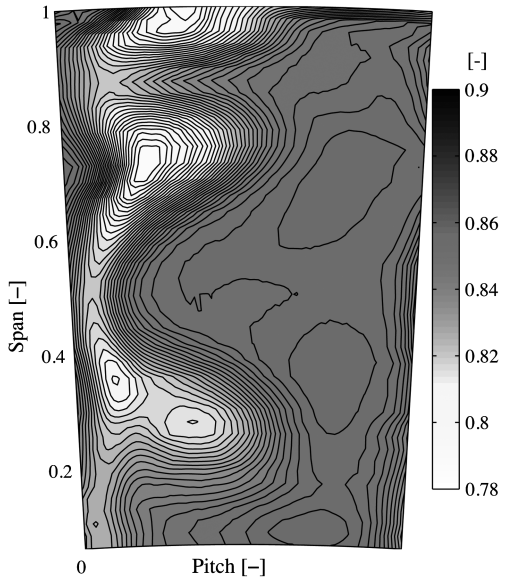

a) Measured

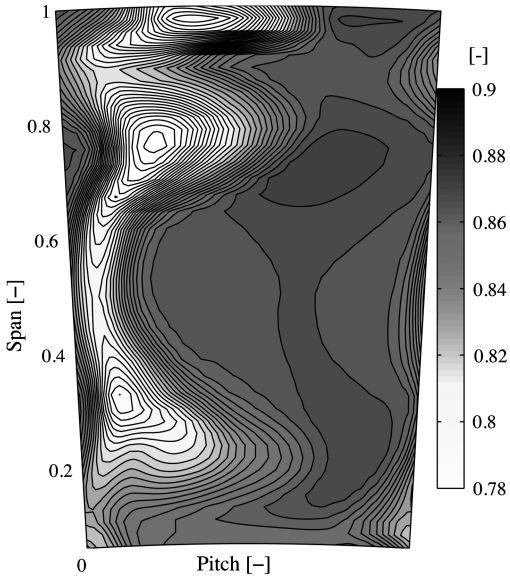

b) Computation

Fig. 12 Comparison of nondimensional relative total pressure for computation and experiment at rotor exit IR = 0.9%.

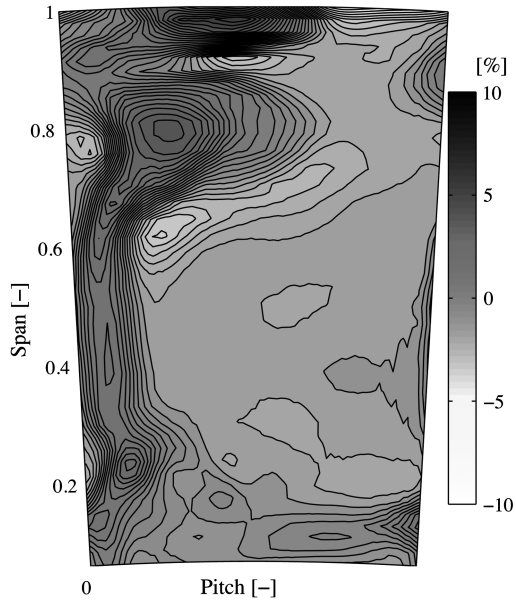

a) IR = -0.1%

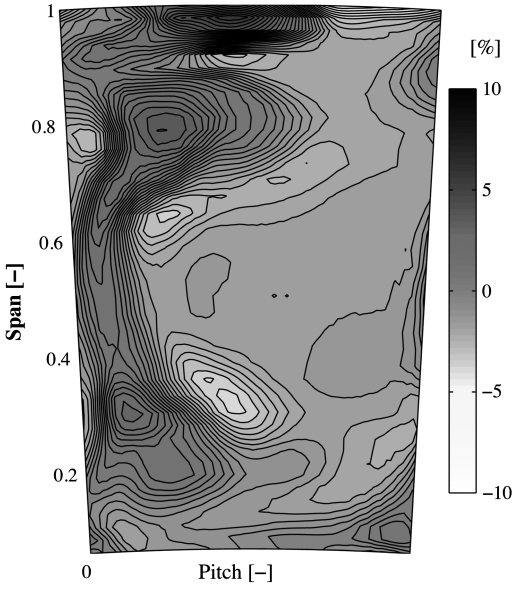

b) IR = 0.9%

Fig. 13 Calculated relative error of computation *Z*.

If Fig. 16 is consulted, one sees a static pressure field at the rim seal exit that is much less rotor-dominated if no purge flow is applied. Instead of the six inclined bands of high and low pressure seen in Fig. 14, the pressure field was now characterized by four vertical high- and low-pressure bands. With purge flow, a strong feedback mechanism was observed in terms of the pressure field. Ingestion and ejection were determined by the pressure field; however, at the same time, the pressure field was changing strongly due to purge flow.

As the stagnation temperature of the injected fluid is 5 K lower than the freestream, the isosurfaces of temperature give a good idea of the injection jet shape. To provide better conservation with the influence of radial migration of the injected fluid, isosurfaces of the rotary temperature T_{trot} at 319 K and not the relative stagnation temperature are plotted in Fig. 17. The definition of the rotary temperature is given as follows:

$$T_{trot} = T_t - ((U \cdot C_\theta)/c_p) \tag{4}$$

The rotor dominated the pressure field, as seen in Fig. 14. Therefore, the injection jets traveled with the rotor and were modulated by the vane pressure field. The jets left the rim seal at the suction side corner of the rotor blades. The IR = 0.9% case showed the least modulation of the low-pressure traces of all the injection cases. Therefore, the jets were well pronounced independent of the vane relative position. The second harmonic seen in the IR = 0.9% case pressure field introduced a second jet, as seen in the middle passage of Fig. 17b. The IR = 0.5% case showed the strongest modulation of the jet caused by the vane pressure field. The first passage, as seen in Fig. 17a, showed a small pronounced jet, the middle passage showed something more like a layer, and the third passage showed hardly any injection. The IR = 1.3% case showed a similar behavior as the IR = 0.9% case, however, with less pronounced jets.

To assess the influence of the injection, a meridional cut was done through the injection region of the central passage. Figure 18 shows the circumferential vorticity within this plane. The suction case is given in Fig. 18a and shows only one vortical structure of positive vorticity, which is the horseshoe vortex 1. If a 0.5% injection was applied, an additional zone of positive vorticity 3 appeared upstream of the horseshoe vortex. If the injection rate was further increased to 0.9%, a further zone of negative vorticity, labeled 2, was generated that was on top of vortex 3. At the maximal injection rate 1.3%, the

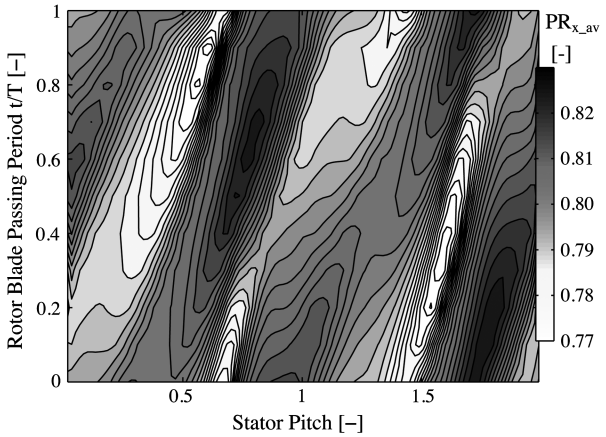

a) IR = 0.5%

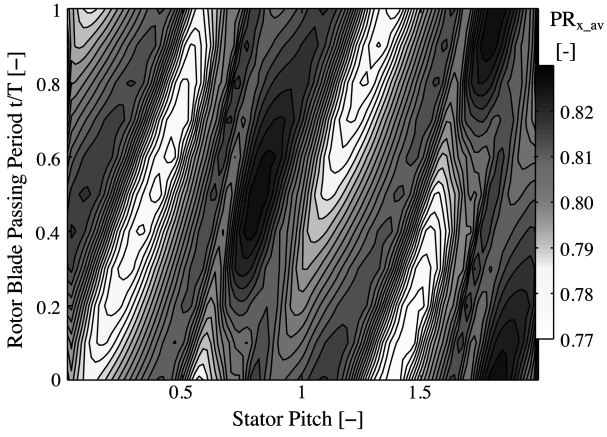

b) IR = 0.9%

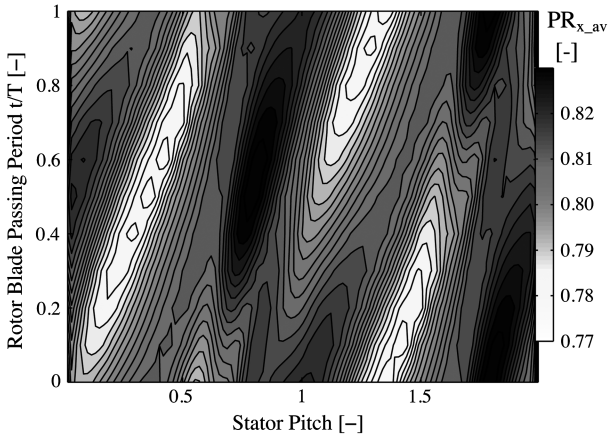

c) IR = 1.3%

Fig. 14 Computational time–space diagram of axially averaged rim seal exit static pressure with purge flow.

horseshoe vortex 1 moved upstream and started to merge with vortex 3. Additionally, zone 2 became stronger.

Figure 19 shows the axial vorticity in a plane at 35% rotor axial chord downstream of the leading edge. Figure 19a shows four

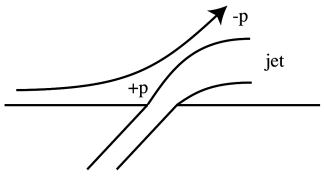

Fig. 15 Illustration of blockage effect of the injection jet.

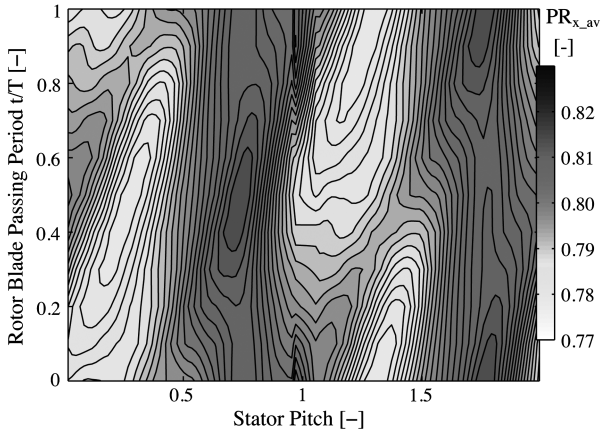

Fig. 16 Computational time–space diagram of axially averaged rim seal exit static pressure without purge flow.

vortical regions depending on the relative vane blade position. The vortex labeled 1 is the pressure side limb of the rotor horseshoe vortex, which becomes the rotor passage vortex. When the hub passage vortex of the first vane row wraps around the rotor leading edge, a pressure and suction side leg evolve, seen as regions 2 and 3. The pressure side leg 2 has the same sense of rotation as the rotor horseshoe vortex pressure side leg. At the suction side, there is a region of negative axial vorticity that is the suction side leg of the rotor horseshoe vortex 4. With injection, an additional zone of positive vorticity with the same sense of rotation as the rotor passage vortex appeared in all three passages simultaneously at the blade suction side above the rotor horseshoe pressure side leg labeled A, B, and C. This was the result of the injection vortices observed at the leading edge. The whole computed rotor domain consisting of three rotor passages is plotted in Fig. 19. As the vane blade relationship is 2:3, all three rotor passages were in a different vane relative position. The geometrical relationship is seen in Fig. 20, which displays a three-dimensional view of the first stage at $t/T = 0$. Additionally, the

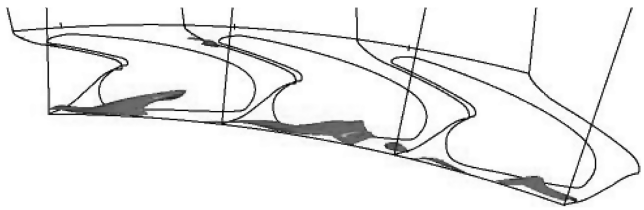

a) IR = 0.5%

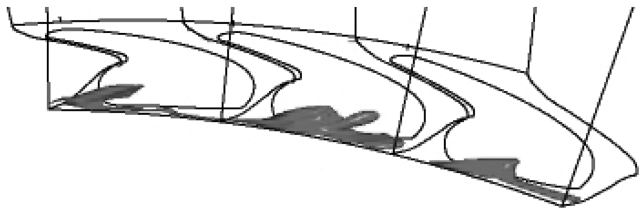

b) IR = 0.9%

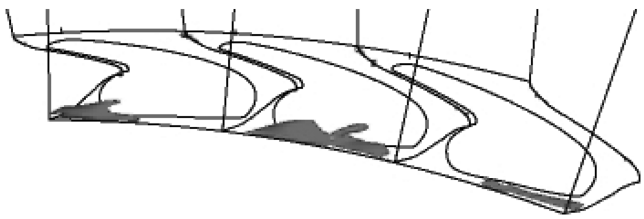

c) IR = 1.3%

Fig. 17 Isosurface of rotary stagnation temperature T_{trot} of 319 K from computation.

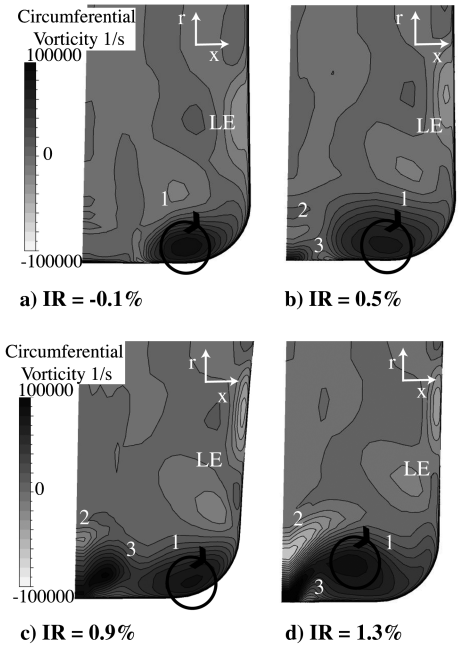

Fig. 18 Circumferential vorticity in a meridional plane cutting through the injection jet.

plane at 35% rotor axial chord downstream of the leading edge is displayed as a black surface. The passages are labeled A, B, and C, corresponding to the vortices in Fig. 19. As a consequence of the different vane blade position of passages A, B, and C, the shape and strength of the injection jets changed, as seen in Fig. 17, and with them the vorticity. As seen in Fig. 19, the vorticity field was not responding linearly to the injection rate. The three cases showed especially a different response regarding the relative stator–rotor

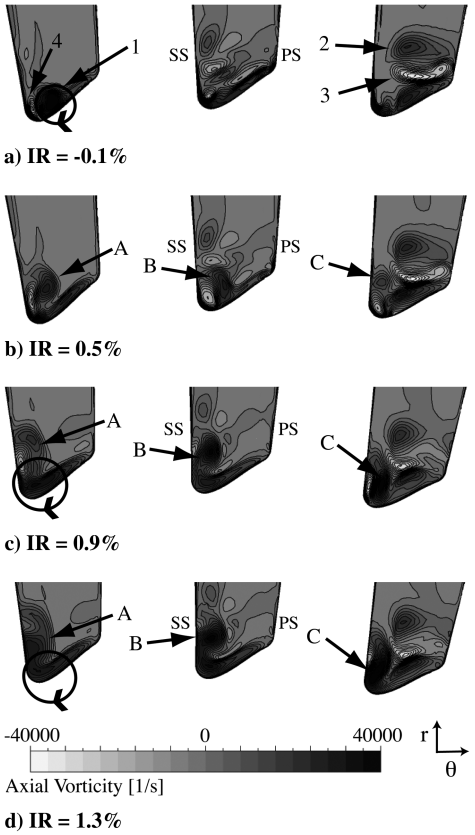

Fig. 19 Computational axial vorticity on an axial plane at 35% rotor axial chord at $t/T = 0$.

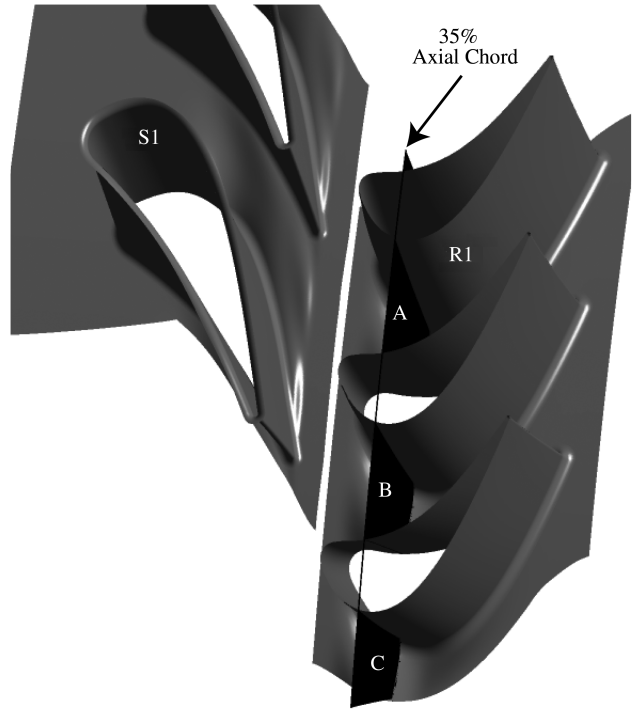

Fig. 20 Geometrical relationship at $t/T = 0$ and the axial plane at 35% rotor axial chord.

position. At the lowest injection rate of 0.5%, the leakage vortex was strong in situation A and weak in situation C. In the other two cases it is the opposite. The effect of increasing the injection rate from 0.5 to 0.9% had a much bigger effect than increasing the injection rate by the same amount from 0.9 to 1.3%. This confirmed the experimental evidence, in which a change of mode happened around an injection rate of 0.9%. The suction side leg of the horseshoe vortex 4 was also strongly influenced by the injection rate. The stronger the injection, the further out and the weaker this vortical structure became.

As reported by Dubief and Delcayre [20], Q isosurfaces turn out to display well coherent vortex structures. Q is defined as

$$Q = \tfrac{1}{4}(\Omega^2 - 2S^2) \tag{5}$$

The value of Q has to be positive according to the Q criterion, which is a necessary condition for the existence of low-pressure vortical tubes. Figure 21 shows isosurfaces of $Q = 10^7$ [1/s^2] of three blade passages in a downstream view with contours of the circumferential vorticity. Additionally, the same axial plane at 35% axial chord as

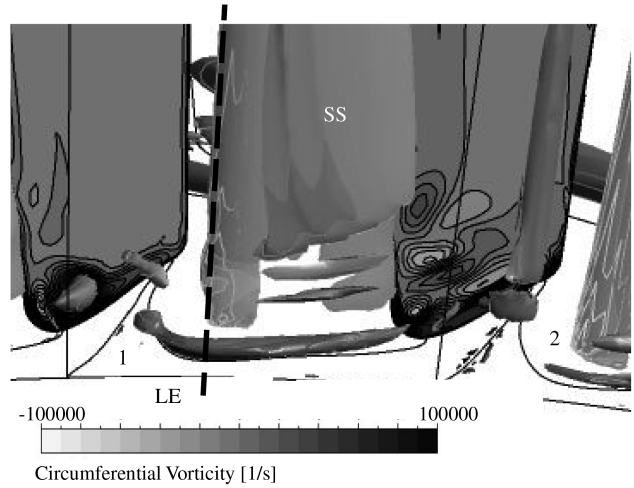

Fig. 21 Computational Q factor (one per second squared) isosurface for suction case IR $= -0.1\%$ at $t/T = 0$.

shown in Fig. 19 is plotted. The dotted line indicates the location of the meridional plane as plotted in Fig. 18. Region 1 shows the pressure side leg of the rotor blade horseshoe vortex. Region 2 shows the horseshoe vortex of the following blade. The vortices created by the injection can be seen in regions 3 and 4 of Fig. 22, which are absent in Fig. 21. Structure 4 is a vortex rotating anticlockwise in the meridional plane, as seen in Fig. 18 and indicated by the dotted line. Structure 3 is rotating clockwise in the same sense as the rotor horseshoe vortex 1. In the 35% axial chord plane, the influence of the anticlockwise vortex 4 was much stronger than the influence of vortex 3, as seen in Figs. 19 and 22. The vortex tube 5 shows the purge-flow-induced vortex of the following passage. The 0.5% case showed much more modulation of the purge-flow-induced vortical structures depending on the vane relative position when comparing 4 and 5. In situation 4, the vortex tube cut through the circumferential plane at a lower radial position than in situation 5. Furthermore, the corotating injection vortex was very weak at this injection rate compared with the higher injection rates. The two higher injection rate cases showed two structures in situation 5 compared with only one tube at 0.5% injection. This was the result of the second harmonic of the static pressure field at the rim seal exit (Fig. 14). Furthermore, vortex 3 was more developed at the two higher injection rates and even additional vortical structures were in the vicinity of vortex 3. Overall it can be stated that the vortical flow structures changed much more going from IR = 0.5 to 0.9% than going from IR = 0.9 to 1.3%, as the flowfields at IR = 0.9 and 1.3% looked very similar.

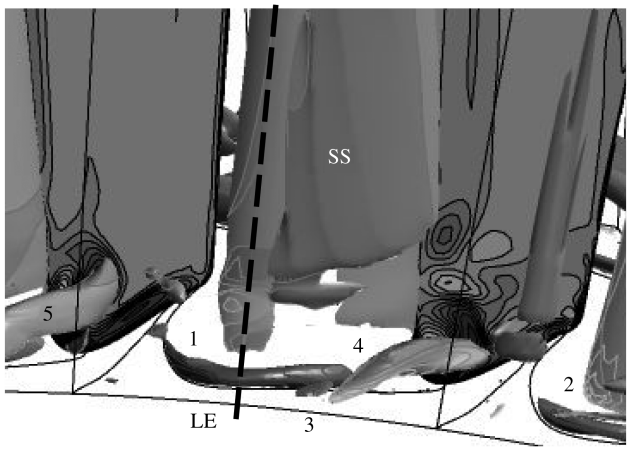

a) IR = 0.5%

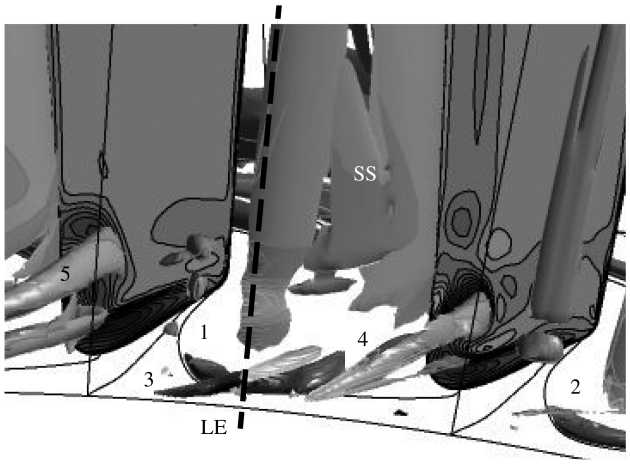

b) IR = 0.9%

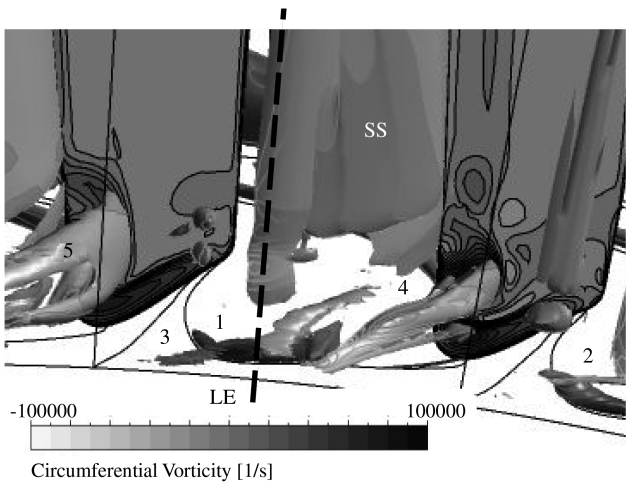

c) IR = 1.3%

Fig. 22 Computational Q factor isosurface for injection cases at $t/T = 0$.

V. Conclusions

This paper presents an efficiency correlation of a high-work turbine for different rates of purge flow. If the injection rate was increased, the hub secondary flow went through a kind of transition at an injection rate of 0.9%. Below this injection rate (0.5%), the injection caused a stronger passage vortex, which remained close to the end wall. At 0.9%, the hub passage vortex increased in size and, at the same time, the integrated rms values rose by 16%. During this transition, subharmonic frequencies appeared that were only present at an injection rate of 0.9%. If the injection rate was further increased, the hub passage vortex reestablished itself at a higher radial position. As a consequence of this transition, the efficiency correlation showed a change of the slope, increasing from 0.7% per injected mass flow percent to 1%.

The rim seal exit pressure field from the computation showed a dominating influence of the rotor once purge flow was present. Furthermore, the IR = 0.9% case showed the least influence of the stator row as well as the appearance of a second harmonic. The injection created normal vorticity at the leading edge, which became streamwise as it was turned around the rotor leading edge. Increasing the injection rate from 0.5 to 0.9% had a much stronger effect in terms of introduced vorticity by the injection vortices than increasing the injection by the same amount from 0.9 to 1.3%. At an injection rate of 0.9%, the rim seal exit pressure field showed a second harmonic, which introduced a second injection jet. With this, additional vorticity was created, which lead to a more diffused hub passage vortex. The injection vortices merged with the rotor hub passage vortex until the exit of the rotor. Therefore, the hub passage vortex showed a strong influence by the injection. Overall the paper has shown that the flowfield does not respond linearly to an increase in purge flow. It remains to be determined if the observations made are generic or if they are associated with this specific end wall geometry. The gained knowledge is of high importance for the creation of purge flow models, which become indispensable if non-axisymmetric end walls are designed in a purge flow environment.

Acknowledgment

The work leading to the results of this paper was carried out within the joint industrial and academic research program that is part of the Luftfahrtforschungsprogramm LuFo3 supported by the German Federal Ministry of Economics and Technology.

References

[1] Kobayashi, N., Matsumato, M., and Shizuya, M., "An Experimental Investigation of a Gas-Turbine Disk Cooling System," *Journal of Engineering for Gas Turbines and Power*, Vol. 106, No. 1, 1984, pp. 136–141.

[2] Chew, J. W., Dadkhah, S., and Turner, A. B., "Rim Sealing of Rotor-Stator Wheelspaces in the Absence of External flow," *Journal of Turbomachinery*, Vol. 114, No. 2, 1992, pp. 433–438. doi:10.1115/1.2929162

[3] Dadkhah, S., Turner, A. B., and Chew, J. W., "Performance of Radial Clearance Rim Seals in Upstream and Downstream Rotor-Stator Wheelspaces," *Journal of Turbomachinery*, Vol. 114, No. 2, 1992, pp. 439–445. doi:10.1115/1.2929163

[4] Roy, R. P., Xu, G., Feng, J., and Kang, S., "Pressure Field and Main-Stream Gas Ingestion in a Rotor-Stator Disk Cavity," American Society of Mechanical Engineers Paper 2001-GT-0564, 2001.

[5] McLean, C., Camci, C., and Glezer, B., "Mainstream Aerodynamic Effects Due to Wheelspace Coolant Injection in a High-Pressure Turbine Stage: Part I-Aerodynamic Measurements in the Stationary Frame," *Journal of Turbomachinery*, Vol. 123, No. 4, 2001, pp. 687–696. doi:10.1115/1.1401026

[6] McLean, C., Camci, C., and Glezer, B., "Mainstream Aerodynamic Effects Due to Wheelspace Coolant Injection in a High-Pressure Turbine Stage: Part II-Aerodynamic Measurements in the Rotational Frame," *Journal of Turbomachinery*, Vol. 123, No. 4, 2001, pp. 697–703. doi:10.1115/1.1397303

[7] Girgis, S., Vlasic, E., Lavoie, J.-P., and Moustapha, S. H., "The Effect of Secondary Air Injection on the Performance of a Transonic Turbine Stage," American Society of Mechanical Engineers Paper GT-2002-30340, 2002.

[8] Ong, J. H. P., Miller, R. J., and Uchida, S., "The Effect of Coolant Injection on the Endwall Flow of a High Pressure Turbine," American Society of Mechanical Engineers Paper GT2006-91060, 2006.

[9] Paniagua, G., Denos, R., and Almeida, S., "Effect of the Hub Endwall Cavity Flow on the Flow-Field of a Transonic High-Pressure Turbine," *Journal of Turbomachinery*, Vol. 126, No. 4, 2004, pp. 578–586. doi:10.1115/1.1791644

[10] Boudet, J., Hills, N. J., and Chew, J. W., "Numerical Simulation of the Flow Interaction Between Turbine Main Annulus and Disc Cavities," American Society of Mechanical Engineers Paper GT2006-90307, 2006.

[11] Reid, K., Denton, J., Pullan, G., Curtis, E., and Longley, J., "The Effect of Stator-Rotor Hub Sealing Flow on the Mainstream Aerodynamics of a Turbine," American Society of Mechanical Engineers Paper GT2006-90838, 2006.

[12] Marini, R., and Girgis, S., "The Effect of Blade Leading Edge Platform Shape on Upstream Disk Cavity to Mainstream Flow Interaction of a High-Pressure Turbine Stage," American Society of Mechanical Engineers Paper GT2007-27429, 2007.

[13] Schuepbach, P., Rose, M. G., Abhari, R. S., Germain, T., Raab, I., and Gier, J., "Effects of Suction and Purge-Flow on Secondary Flow Structures of a High-Work Turbine," American Society of Mechanical Engineers Paper GT2008-50471, 2008.

[14] Germain, T., Nagel, M., Raab, I., Schuepbach, P., Rose, M. G., and Abhari, R. S., "Improving Efficiency of a High Work Turbine Using Non-Axisymmetric Endwalls. Part I: Endwall Design and Performance," American Society of Mechanical Engineers Paper GT2008-50469, 2008.

[15] Schuepbach, P., Rose, M. G., Abhari, and Gier, J., "Influence of Rim Seal Purge Flow on Performance of an Endwall-Profiled Axial Turbine," American Society of Mechanical Engineers Paper GT2009-59653, 2009.

[16] Behr, T., Kalfas, A. I., and Abhari, R. S., "Unsteady Flow Physics and Performance of a One-and-1/2-Stage Unshrouded High Work Turbine," *Journal of Turbomachinery*, Vol. 129, No. 2, 2007, pp. 348–359. doi:10.1115/1.2447707

[17] Kupferschmied, P., Kopperl, O., Gizzi, W. P., and Gyarmathy, G., "Time Resolved Flow Measurements with Fast Aerodynamic Probes in Turbomachinery," *Measurement Science and Technology*, Vol. 11, 2000, pp. 1036–1054. doi:10.1088/0957-0233/11/7/318

[18] Pfau, A., Schlienger, J., Kalfas, A. I., and Abhari, R. S., "Unsteady, 3-Dimensional Flow Measurement Using a Miniature Virtual 4 Sensor Fast Response Aerodynamic Probe (FRAP)," American Society of Mechanical Engineers Paper GT2003-38128, 2003.

[19] Porreca, L., Hollenstein, M., Kalfas, A. I., and Abhari, R. S., "Turbulence Measurements and Analysis in a Multistage Axial Turbine," *Journal of Propulsion and Power*, Vol. 23, No. 1, 2007, pp. 227–234. doi:10.2514/1.20022

[20] Dubief, Y., and Delcayre, F., "On Coherent-Vortex Identification in Turbulence," *Journal of Turbulence*, Vol. 1, No. 1, 2000, p. 11. doi:10.1088/1468-5248/1/1/011

A. Prasad
Associate Editor